Supplemental Document

Biomedical Optics EXPRESS

# Layer-based, depth-resolved computation of attenuation coefficients and backscattering fractions in tissue using optical coherence tomography: supplement

**Taylor M. Cannon,[1,2,*] Brett E. Bouma,[1,2] and Néstor Uribe-Patarroyo[2]**

[1] *Massachusetts Institute of Technology, Institute of Medical Engineering and Science, 70 Massachusetts Avenue, Cambridge, MA 02141, USA*
[2] *Wellman Center for Photomedicine, Massachusetts General Hospital, 40 Blossom St, Boston, MA 02114, USA*
[*] *cannont@mit.edu*

This supplement published with The Optical Society on 20 July 2021 by The Authors under the terms of the Creative Commons Attribution 4.0 License in the format provided by the authors and unedited. Further distribution of this work must maintain attribution to the author(s) and the published article's title, journal citation, and DOI.

Supplement DOI: https://doi.org/10.6084/m9.figshare.14955507

Parent Article DOI: https://doi.org/10.1364/BOE.427833

# Layer-based, depth-resolved computation of attenuation coefficients and backscattering fractions of tissue using optical coherence tomography: supplemental document

Data were simulated for Figure S1 based on input values for scattering particle diameter, concentration, and refractive index representative of typical values in tissue settings. Particle size varied from 0.5 to 5 µm diameter to encompass both smaller (mitochondria, lysosomes) and larger (nuclei) organelles. The incident light wavelength was held constant at 1.3 µm, and the ambient refractive index was held constant at 1.34 (the group refractive index for water at a 1.3 µm illumination wavelength [1]). Refractive indices of 1.38 and 1.46 were chosen as two representative values for scatterers found in epithelial tissues. Previously reported values for nuclei range from 1.36 to 1.38 [2–4], though values as high as 1.44 have been reported when including the nucleolus [2, 4], and mitochondrial values have been reported at 1.4 [4, 5]. Refractive indices for other organelles such as lysosomes have been reported as high as 1.6 [6], but we assume their contribution to the overall scattering signal will be low for most epithelial tissues compared to that of nuclei and mitochondria [7]. The resulting plots show the variability of the concentration dependent attenuation coefficient ($\mu_{\text{dep}}$) and backscattering fraction values for the input parameters. Attenuation coefficient values were calculated accounting for concentration dependence [8] over volume fractions ranging from 0.001 to 0.025, with $\mu_{\text{dep}}$ increasing with increasing volume fraction. Since $\alpha$ is not dependent on concentration, a single curve was output to demonstrate the dependence of this parameter on scattering particle diameter and refractive index.

Figure S2 outlines the intermediate results outputted at each step of our custom segmentation scheme for finding nuclear concentration (e.g., NCR) and size. The Trainable Weka Segmentation plugin [9] was used in ImageJ to isolate the epithelium of input high-resolution digital pathology images (a) as the region of greatest interest by masking out background and lamina propria layers (b, c). We used a number of built-in image processing functions in MATLAB to subsequently perform segmentation of nuclei. Firstly, a Wiener filter was used to smooth the input image. Next, a threshold was applied to the first channel of the filtered RGB image to isolate nuclei. The functions `imclose`, `imfill`, and `bwareaopen` (Image Processing toolbox) were used to eliminate extraneous non-nuclear pixels that had not been cleared by initial thresholding. To prevent adjacent nuclei from being counted as a single nucleus, the resulting binary map was prepared with `imextendedmax` and `imimposemin` for analysis with the `watershed` transform. The watershed output was converted back to a map with `label2rgb`. These intermediate results can be visualized for a larger ROI in (d), and for two smaller ROIs of differing nuclear density in (e) and (f). The full map resulting from these pre-processing steps, complementary in size to the input image in (a), is shown as a binary map in (g). To calculate nuclear density, or effectively the nuclear-cytoplasmic ratio, `imfilter` was used to find locally averaged total areas of nuclei. This was divided by the total area of tissue, analogous to the blue epithelial mask in (b), to output the nuclear density map in (h). Finally, individual nuclei were counted using Centroid data determined by applying `regionprops` to the full map of traced nuclei. Sizes of individual nuclei in units of pixels were calculated as $N_{\text{size, px}} = \frac{A_n}{N_n}$, where $A_n$ is total area of all nuclei and $N_n$ is the total number of nuclei. We converted $N_{\text{size, px}}$ to physical units by applying a pixel-to-µm conversion factor determined from the input high-resolution digital pathology images. The diameters of individual nuclei were calculated as $N_{\text{diameter},\mu m} = 2\sqrt{\frac{N_{\text{size},\mu m}}{\pi}}$. Similarly to (h), local smoothing of determined diameters was performed with `imfilter` to produce the nuclear diameter map in (i).

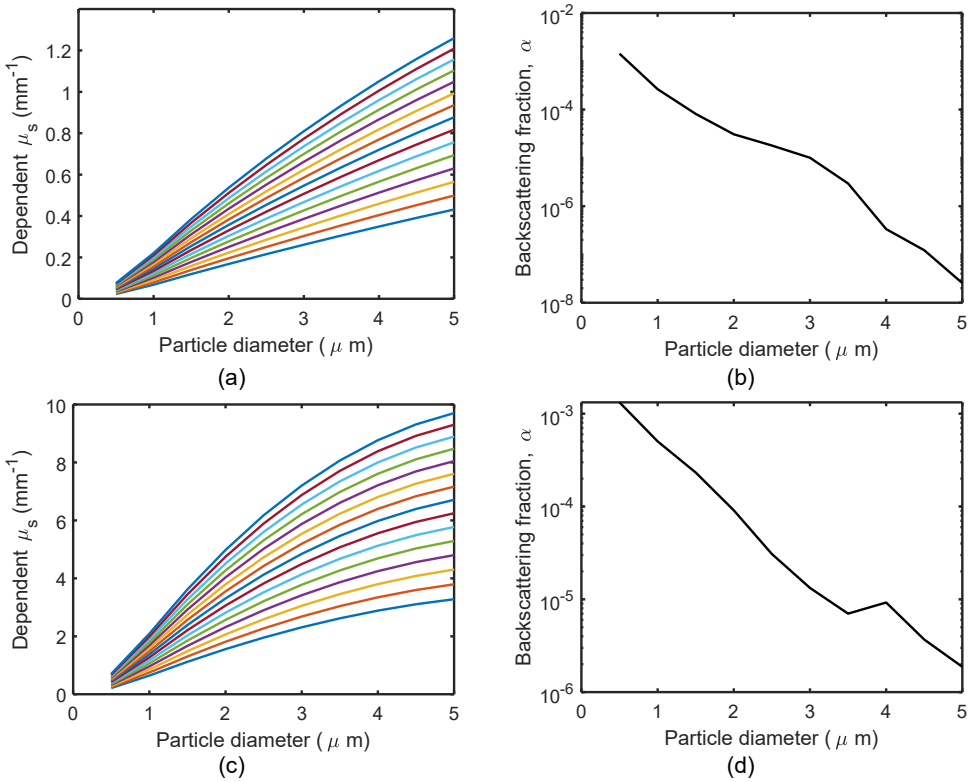


Fig. S 1. Representative variation in $\alpha$ and $\mu$ values with respect to particle size, concentration, and refractive index. A particle refractive index of 1.38 is used for calculations in (a, b), and a higher index of 1.46 is used for (c, d). The ambient refractive index assumed for each is 1.34. In the case of each refractive index, the concentration-dependent $\mu_s$, calculated for volume fractions ranging from 0.001 to 0.025, has a lower overall range of values than the resulting $\alpha$ values, which vary over several orders of magnitude.

To realize our layer-based method for calculating $\mu(z)$ and $\alpha$, we implemented automated segmentation as described in Section 2.6. Figure S3 visualizes the boundaries which were detected on an A-line by A-line basis based on changes in the magnitude and slope of the intensity decay. Here, these are shown for each A-line as a map discriminating what our methods identified as discrete layers in the porcine GI tissue samples with representative $\mu_{\text{fit}}$ and over which $\alpha$ is constant. The same methods were also applied to the layered phantoms shown in Figure 3, but for these, only two layers were identified, and this is more simply visualized from the fitting overlaid on the A-line in Fig. 3(a).

We performed further analysis to gain greater insight into the impact of OCT system design parameters on the amount of multiply scattered signal detected, particularly with respect to the confocal and coherence gating, each of which are known to reduce the amount of multiply scattered light detected (Fig. S4). For a sample of Intralipid at relatively high concentration (4%, $v_f$ =0.044), data were acquired for the same sample ROI [see panel (a)] at three different NAs ranging from 0.05 to 0.1 to study the confocal gate impact. To study the coherence gate impact, the signal spectrum was windowed at its full extent, 1/4 of the spectrum, and 1/8 of the spectrum, altering the tomogram axial resolution. The varying speckle patterns resulting from

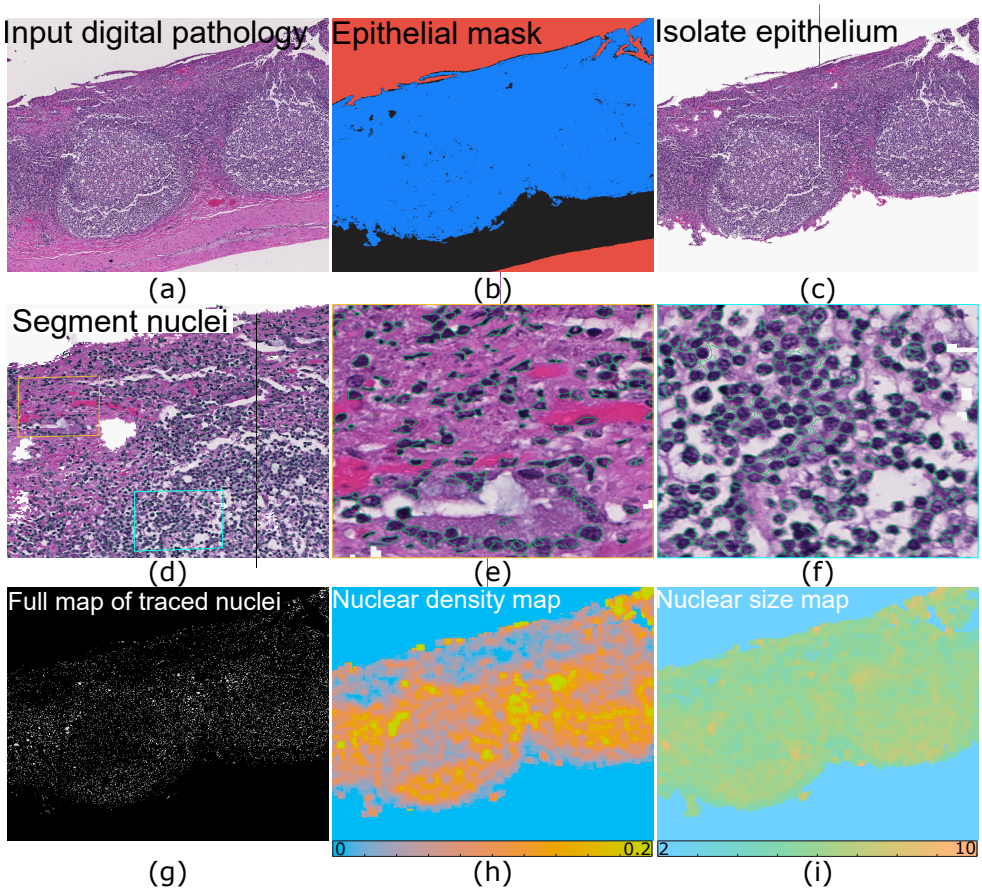


Fig. S2. Overview of processing steps in custom methods for nuclear segmentation in digital pathology images. Using a trainable segmenter in ImageJ [9], masks were generated (b) using an input high-resolution digital pathology image (a) which were applied to the input image to mask the epithelium as the layer of interest (c). Within the epithelium, a series of binary thresholding, smoothing, and filtering steps were used to identify nuclei, as show in a large ROI (d) and two smaller ROIs (e, f) as indicated within (d). The full map (g) was used to calculate nuclear cytoplasmic ratio as an indicator of nuclear particle density (h) and local nuclear diameter in μm (i).

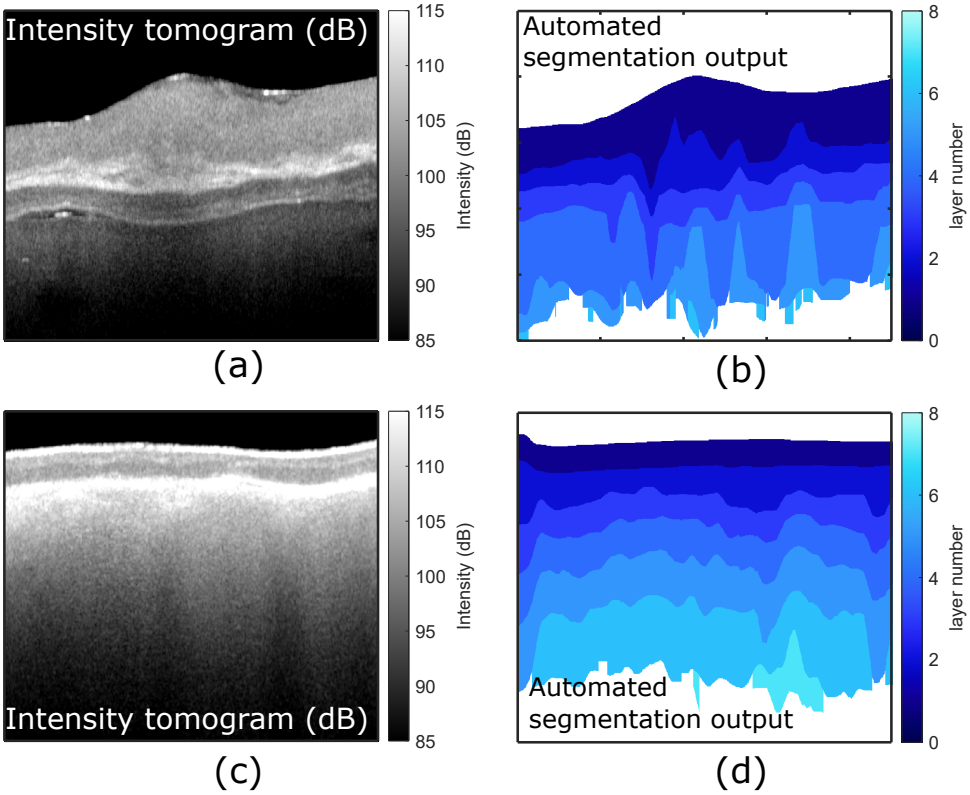


Fig. S3. Automated segmentation results for tissue cross sections shown in Figure 6 (a) and Figure 7 (b) of the manuscript. As described in methods, layers in tissue were discriminated based on features of the intensity decay on an A-line by A-line basis, with the minimum axial extent of a layer in this application set to 108 µm.

the NA alteration and spectral window alteration are shown in panels (b) and (c) respectively. The resulting lateral point spread functions from the three NAs and the resulting axial PSF from the three spectral windows are shown in panels (d) and (e) respectively. Following reconstruction, tomogram intensities were corrected to account for the variable confocal functions with the different NA used to acquire the data. In the resulting intensity decays, the NA-diverse signals differed with respect to each other in decay rate at depths greater than 1 mm, with the low NA (0.05) measurement having the least steep decay at these depths. This corresponds to a greater amount of multiple scattering affecting the signal in this axial region than the higher NA measurements, which agrees with better rejection of multiple scattering with higher NA and thus stronger confocal gating. The differences in intensity decay between signals of varying axial resolution were minimal throughout the entirety of the decay, suggesting that the coherence gate has less impact on detection of multiply scattered light than the confocal gate.

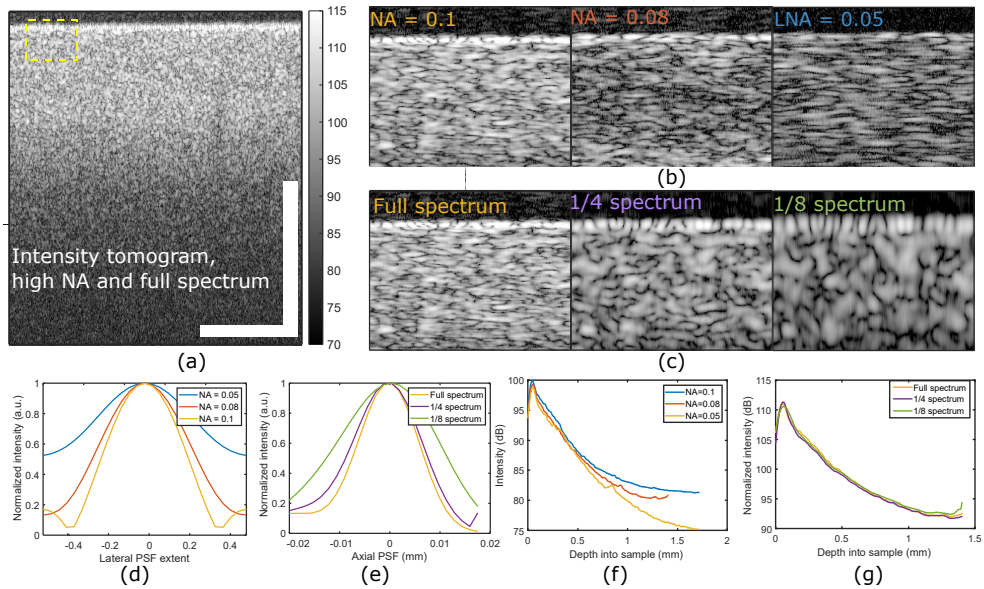


Fig. S4. Comparison of the impact of the coherence gate on the amount of multiply scattered light detected from a sample. For a sample of concentrated 4 % Intralipid (a), data were acquired at three different NA, the changing speckle pattern of each is shown in (b). Hanning windows of variable sizes were aplied to the tomogram spectrum to generate different effective axial resolutions (c). The normalized lateral PSF for each acquired NA (d) and the axial PSF for each spectral window (e) are displayed. Varying the confocal gate had a greater impact on the shape of the confocal-corrected intensity decay, particularly at greater sample depths likely to be affected by multiple scattering (f) than did varying the coherence gate (g).

## References


1. V. M. Kodach, D. J. Faber, J. van Marle, T. G. van Leeuwen, and J. Kalkman, "Determination of the scattering anisotropy with optical coherence tomography," Opt. Express **19**, 6131 (2011).
2. W. Choi, C. Fang-Yen, K. Badizadegan, S. Oh, N. Lue, R. R. Dasari, and M. S. Feld, "Tomographic phase microscopy," Nat Methods **4**, 717–719 (2007).
3. M. Schürmann, J. Scholze, P. Müller, J. Guck, and C. J. Chan, "Cell nuclei have lower refractive index and mass density than cytoplasm," J. Biophoton **9**, 1068–1076 (2016).
4. H. Zhang, Z. A. Steelman, D. S. Ho, K. K. Chu, and A. Wax, "Angular range, sampling and noise considerations for inverse light scattering analysis of nuclear morphology," J. Biophotonics **12**, e201800258 (2019).
5. K. Haseda, K. Kanematsu, K. Noguchi, H. Saito, N. Umeda, and Y. Ohta, "Significant correlation between refractive index and activity of mitochondria: Single mitochondrion study," Biomed. Opt. Express **6**, 859 (2015).
6. J. D. Wilson, W. J. Cottrell, and T. H. Foster, "Index-of-refraction-dependent subcellular light scattering observed with organelle-specific dyes," J. Biomed. Opt. **12**, 014010 (2007).
7. V. Backman, M. B. Wallace, L. T. Perelman, J. T. Arendt, R. Gurjar, M. G. Muller, Q. Zhang, G. Zonios, E. Kline, T. McGillican, and M. Feld, "Detection of preinvasive cancer cells," Nature **406**, 35–36 (2000).
8. M. Almasian, N. Bosschaart, T. G. van Leeuwen, and D. J. Faber, "Validation of quantitative attenuation and backscattering coefficient measurements by optical coherence tomography in the concentration-dependent and multiple scattering regime," J. Biomed. Opt. **20**, 121314 (2015).
9. I. Arganda-Carreras, V. Kaynig, C. Rueden, K. W. Eliceiri, J. Schindelin, A. Cardona, and H. Sebastian Seung, "Trainable Weka Segmentation: a machine learning tool for microscopy pixel classification," Bioinformatics **33**, 2424–2426 (2017).